Pd–Ir Core–Shell Nanocubes: A Type of Highly Efficient and Versatile Peroxidase Mimic

Xiaohu Xia,*,† Jingtuo Zhang,† Ning Lu,‡ Moon J. Kim,‡ Kushal Ghale,§ Ye Xu,§ Erin McKenzie,† Jiabin Liu,† and Haihang Ye†

†Department of Chemistry, Michigan Technological University, Houghton, Michigan 49931, United States, ‡Department of Materials Science and Engineering, University of Texas at Dallas, Richardson, Texas 75080, United States, and §Department of Chemical Engineering, Louisiana State University, Baton Rouge, Louisiana 70803, United States

ABSTRACT Peroxidase mimics with dimensions on the nanoscale have received great interest as emerging artificial enzymes for biomedicine and environmental protection. While a variety of peroxidase mimics have been actively developed recently, limited progress has been made toward improving their catalytic efficiency. In this study, we report a type of highly efficient peroxidase mimic that was engineered by depositing Ir atoms as ultrathin skins (a few atomic layers) on Pd nanocubes (*i.e.*, Pd–Ir cubes). The Pd–Ir cubes exhibited significantly enhanced efficiency, with catalytic constants more than 20- and 400-fold higher than those of the initial Pd cubes and horseradish peroxidase (HRP), respectively. As a proof-of-concept demonstration, the Pd–Ir cubes were applied to the colorimetric enzyme-linked immunosorbent assay (ELISA) of human prostate surface antigen (PSA) with a detection limit of 0.67 pg/mL, which is ~110-fold lower than that of the conventional HRP-based ELISA using the same set of antibodies and the same procedure.

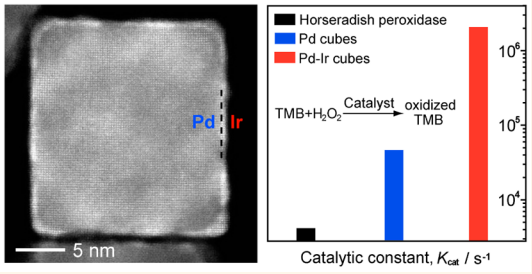

KEYWORDS: iridium · nanocrystal · peroxidase mimic · catalytic efficiency · immunoassay

Peroxidases are a family of enzymes that catalyze the oxidation of certain compounds with peroxides (H_2O_2 in most cases). They are known to play vital roles in biological systems such as detoxifying H_2O_2 in human bodies and defending against pathogens in plants.[1,2] Significantly, peroxidases can be isolated from organisms and applied to many areas such as biomedicine and environmental protection. Taking horseradish peroxidase (HRP) as an example, they are usually extracted from horseradish roots and have been widely used in diagnostics and imaging, wherein HRPs are conjugated to antibodies and specifically generate color signals by catalyzing colorimetric substrates.[3] HRP has also found use in the treatment of industrial wastewater owing to its capability in promoting the conversion of toxic pollutants such as phenols into harmless substances.[4] Despite these current uses, extensive implementation of peroxidases into practical applications remains a grand challenge mainly due to their relatively poor stabilities and the difficulties of isolation and purification.

To circumvent the aforementioned issues, artificial peroxidases (*i.e.*, peroxidase mimics) as alternatives to natural peroxidases have been developed in recent years.[5] The first example of peroxidase mimics was reported by Yan and co-workers in 2007 with the discovery of peroxidase-like activity of Fe_3O_4 magnetic nanoparticles.[6] Shortly thereafter, a number of inorganic nanomaterials including those made of metal oxides (*e.g.*, Fe_2O_3, Co_3O_4, and V_2O_5), carbon materials, noble metals (*e.g.*, Pd and Pt), and a combination of them were reported to show similar peroxidase-like properties.[7−15] Unlike natural peroxidases, peroxidase mimics are less vulnerable to denaturation and protease digestion and therefore have proven to be much more stable. In spite of the superior stability of the mimics, improvement in their catalytic efficiency has been met with limited success. Using HRP as a benchmark, most of the previously reported peroxidase mimics with sizes 1–100 nm show only up

* Address correspondence to xiaxh@mtu.edu.

Received for review June 10, 2015 and accepted September 1, 2015.

Published online September 03, 2015
10.1021/acsnano.5b03525

to 1 order of magnitude increase in efficiency (10^3 *versus* 10^4 s^{-1} in catalytic constant, K_{cat}; see Table S1 for detailed comparison). Moreover, since peroxidase mimics are synthetic nanostructures, it has been challenging to finely control their uniformities (in terms of both shape and size) and to modify their surface with ligands and biomolecules.

Herein, we demonstrate that Pd−Ir core−shell nanocubes are a type of highly efficient peroxidase mimic with K_{cat} at a level as high as 10^6−10^7 s^{-1}, which is approximately 3 orders of magnitude higher than that of HRP (ref 6). The motivations for us to choose Ir-based nanostructures were that (i) Ir could efficiently decompose H_2O_2 as other Pt-group metals did,[16] which is the basis of peroxidase-like activity, and (ii) our recent study, for the first time, has demonstrated an effective approach based on seed-mediated growth to shaping Ir nanocrystals,[17] allowing us to prepare Ir nanocrystals with well-defined shapes. In addition to high efficiency, the new peroxidase mimics have several other promising features that make them attractive for various applications: (i) They could be produced in high purity (>95%) and good uniformity, ensuring reproducible performance; (ii) their sizes can be readily controlled from ~8 to ~52 nm, making them adaptable to desired platforms; (iii) their surfaces can be easily modified with functional groups such as $-NH_2$ and −COOH by means of Ir-thiolate bonding, allowing the convenient labeling of ligands and biomolecules; and (iv) they are made of inert noble metals with good stabilities, enabling them to survive harsh environments. As a proof-of-concept demonstration, the Pd−Ir cubes were applied to the colorimetric immunoassay of human prostate specific antigen (PSA) with a detection limit reaching the level of subpicogram per milliliter.

RESULTS AND DISCUSSION

Structure and Composition Study. We started with the synthesis of Pd−Ir core−shell nanocubes that was conducted using seed-mediated growth. In a standard synthesis, a solution of Na_3IrCl_6 in ethylene glycol was introduced at a rate of 1.0 mL/h (with a syringe pump) into a mixture containing Pd cubes of 18 nm in edge length as the seeds, L-ascorbic acid as a reductant, and poly(vinylpyrrolidone) as a stabilizer, which had been preheated to 200 °C under magnetic stirring (see Methods for experimental details). We chose Pd cubes as the seeds because they are well-defined nanostructures mainly covered by {100} facets, making it convenient to track the subsequent overgrowth of Ir. The 18 nm Pd cubic seeds (Figure S1b) were prepared using a previously reported one-pot synthesis.[18] Figure 1a shows a typical transmission electron microscopy (TEM) image of the Pd−Ir core−shell cubes prepared from a standard synthesis. It can be seen that the cubic shape of the Pd seeds was retained after the growth of Ir. Thin Ir shells (with darker contrast) over

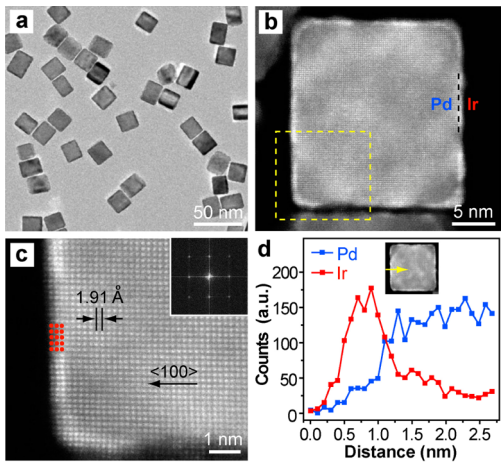

Figure 1. Structural and compositional analyses of the Pd−Ir core−shell cubes that were obtained by depositing Ir atoms on 18 nm Pd cubic seeds. (a) Typical TEM image showing the overall cubic shape and good uniformity of the sample. (b) HAADF-STEM image of an individual particle. (c) Atomic-resolution HAADF-STEM image taken from the corner region marked by a yellow box in (b). Inset is the corresponding Fourier transform pattern. (d) Line-scan EDX spectra of elemental Pd and Ir that were recorded from an individual particle (inset) along an edge-to-edge direction as indicated by the yellow arrow.

the Pd seeds can be resolved by a close examination owing to the difference in atomic number between Ir and Pd. The low-magnification TEM and high-angle annular dark-field scanning TEM (HAADF-STEM) images (Figure S2) demonstrated that the Pd−Ir cubes could be obtained with a high quality. Our analyses on 200 particles indicated that (i) 98.6% of particles displayed well-defined cubic shapes; (ii) the products had a narrow size distribution (1.31 nm in standard deviation); and (iii) the average edge length of the Pd−Ir cubes was 19.2 nm, which was 1.2 nm greater than that of the initial Pd cubic seeds. Therefore, on average, the thickness of the Ir shell deposited on each side face of a Pd cubic seed was about 0.6 nm. Figure 1b shows a HAADF-STEM image taken from an individual Pd−Ir cube, from which a thin Ir shell on the surface of Pd seed is clearly seen (with a brighter contrast). The enlarged atomic-resolution HAADF-STEM image together with its Fourier transform pattern (Figure 1c) reveals the continuous lattice fringes from the Pd core to the Ir shell, indicating an epitaxial relationship between these two elements. Figure 1c also shows that Ir atoms were unevenly coated on the surfaces of Pd seeds with a maximum number of atomic layers of 3, implying the involvement of 3D island growth mode during synthesis as demonstrated in our previous studies.[17,19] Figure 1d shows a line profile of energy-dispersive X-ray spectroscopy (EDX) analysis recorded from an individual Pd−Ir cube, further confirming the elemental compositions of the Ir shell and Pd core. We also quantitatively analyzed the molar ratio of Ir to Pd ($PdIr_x$) for these Pd−Ir cubes using inductively coupled plasma atomic

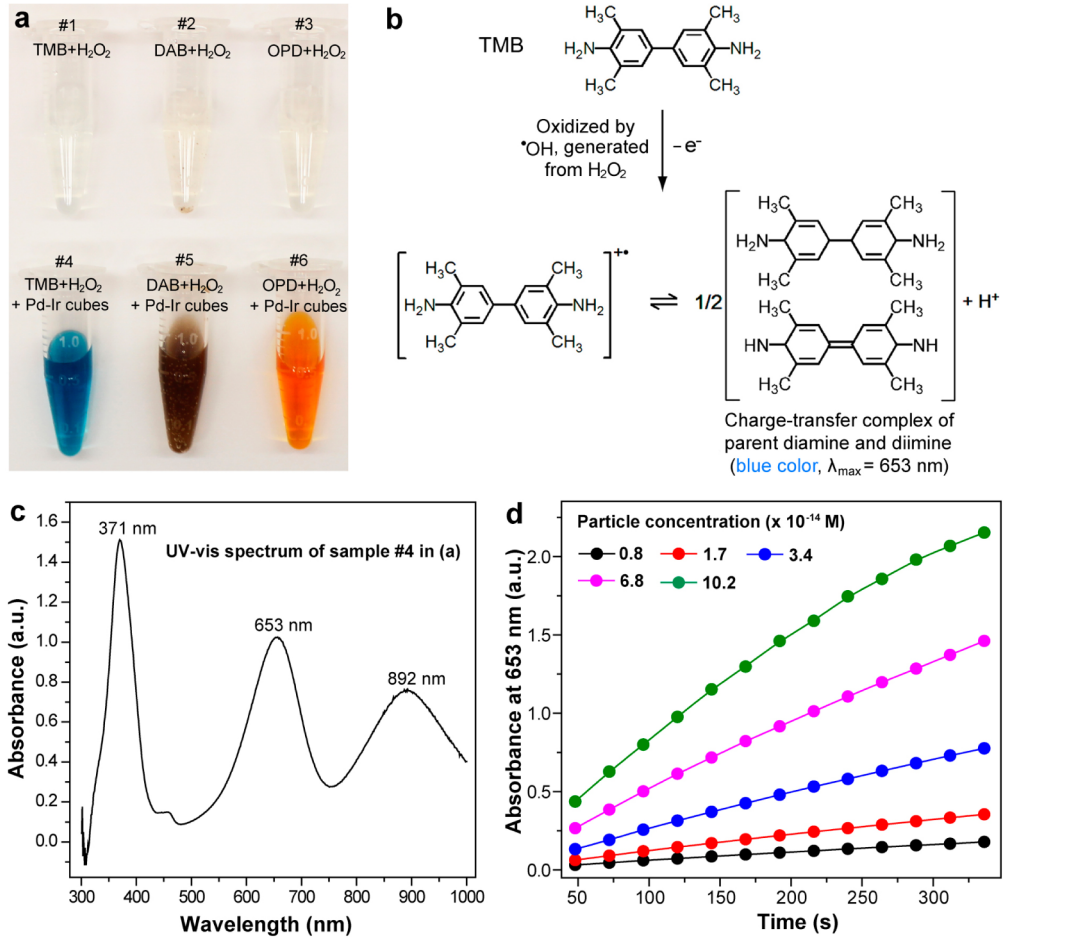

Figure 2. Peroxidase-like activity of Pd−Ir cubes. (a) A photograph taken at the reaction time *t* = 5 min, showing the capability of the 19.2 nm Pd−Ir cubes (~5 × 10^{-14} M) in catalyzing the oxidations of various peroxidase substrates (*i.e.*, TMB, DAB, and OPD) by H_2O_2 that produce colored products. (b) Scheme showing the oxidation of TMB by H_2O_2 to form the blue-colored products. (c) UV−vis spectrum taken from sample #4 in (a). (d) Time- and particle concentration-dependent absorbance at 653 nm measured from the reaction solutions containing 2.0 M H_2O_2, 0.8 mM TMB, and 19.2 nm Pd−Ir cubes of different concentrations in 0.2 M HOAc/NaOAc buffer, pH 4.0 at room temperature.

emission spectroscopy (ICP-AES), which was measured to be $PdIr_{0.062}$. According to the ICP-AES data, the size of Pd cubic seeds, and the unit cell parameters of Ir,[17,20] the average number of Ir atomic layers was estimated to be 1 for this sample, indicating an overall monolayer coating of Ir on the Pd cubic seeds. Since ICP-AES averages over a much larger number of particles than electron microscopy, the analysis of elemental composition for the Pd−Ir cubes is referred to the ICP-AES data in the following discussion.

Peroxidase-like Properties. We then evaluated the peroxidase-like activity of the as-synthesized Pd−Ir cubes. As shown in Figure 2, the Pd−Ir cubes could rapidly catalyze the oxidation of 3,3′,5,5′-tetramethylbenzidine (TMB, a typical HRP substrate[21]) by H_2O_2, yielding a blue-colored product with a maximum absorbance at 653 nm (Figure 2b,c). In addition to TMB, they can also catalyze the oxidation of several other peroxidase substrates such as 3,3′-diaminobenzidine (DAB) and *o*-phenylenediamine (OPD), producing brown- and orange-colored products, respectively (Figure 2a). These results clearly demonstrated the peroxidase-like property of the Pd−Ir cubes. Using the oxidation of TMB by H_2O_2 as a model reaction, we found that the catalytic efficiency of the Pd−Ir cubes (3.4 × 10^{-14} M in particle concentration) is, like other peroxidase mimics, dependent on pH, temperature, and TMB and H_2O_2 concentrations. On the basis of the systematic examination of these factors (see Figure S3), the optimal conditions were found to be pH 4.0, 37 °C, 0.8 mM TMB, and 7.0 M H_2O_2. It should be pointed out that no significant change of activity was observed for temperatures at 10−37 °C and H_2O_2 concentrations at 1.5−7.0 M (see Figure S3). Therefore, for simplicity, we adopted pH 4.0, room temperature (~22 °C), 0.8 mM TMB, 2.0 M H_2O_2, and 3.4 × 10^{-14} M Pd−Ir cubes as the standard conditions for subsequent studies of the 19.2 nm Pd−Ir cubes. As shown in Figure S4, the catalytic activities of the Pd−Ir cubes remained stable after they had been treated with heat (40−200 °C) and acid or base (pH 0−12) for 2 h, indicating their outstanding thermal and chemical stabilities.

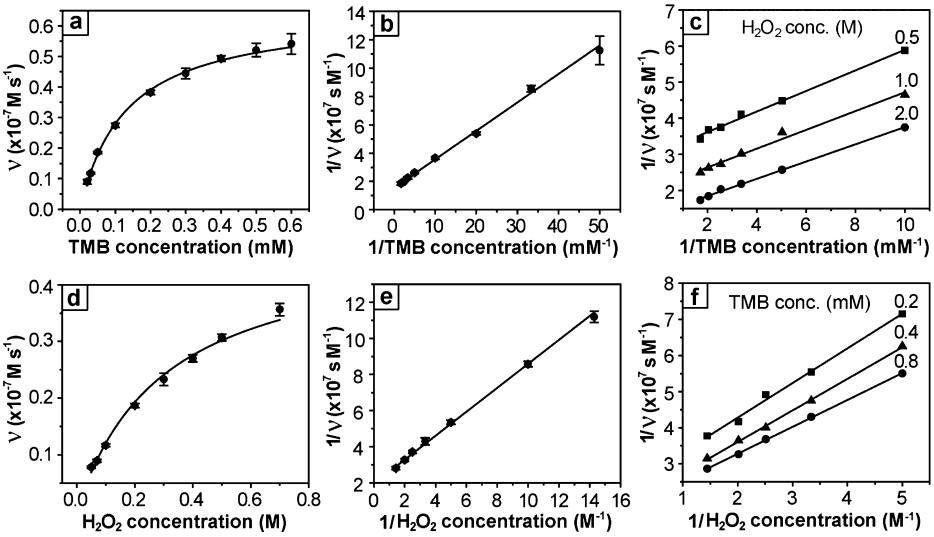

Figure 3. Steady-state kinetic assays of Pd−Ir cubes as catalysts for the oxidation of TMB by H_2O_2. The initial reaction velocity (v) was measured under standard conditions. Error bars indicate the standard deviations of three independent measurements. (a−c) Kinetic assays toward TMB: (a) Plot of v against TMB concentration, in which H_2O_2 concentration was fixed at 2.0 M; (b) double-reciprocal plot generated from (a); (c) double-reciprocal plots at different H_2O_2 concentrations. (d−f) Kinetic assays toward H_2O_2: (d) plot of v against H_2O_2 concentration, in which TMB concentration was fixed at 0.8 mM; (e) double-reciprocal plot generated from (c); (f) double-reciprocal plots at different TMB concentrations.

TABLE 1. Comparison of the Kinetic Parameters of Various Catalysts toward the Oxidation of TMB by H_2O_2[a]

catalyst	[E] (M)	substrate	K_m (M)	V_{max} (M s^{-1})	K_{cat} (s^{-1})
19.2 nm Pd−Ir cubes	3.4×10^{-14}	TMB	1.3×10^{-4}	6.5×10^{-8}	1.9×10^{6}
	3.4×10^{-14}	H_2O_2	3.4×10^{-1}	5.1×10^{-8}	1.5×10^{6}
18 nm Pd cubes	1.4×10^{-12}	TMB	5.4×10^{-5}	9.7×10^{-8}	6.9×10^{4}
	1.4×10^{-12}	H_2O_2	7.0×10^{-1}	6.5×10^{-8}	4.6×10^{4}
HRP (ref 6)	2.5×10^{-11}	TMB	4.3×10^{-4}	1.0×10^{-7}	4.0×10^{3}
	2.5×10^{-11}	H_2O_2	3.7×10^{-3}	8.7×10^{-8}	3.5×10^{3}

[a] [E] represents the catalyst concentration, K_m is the Michaelis constant, V_{max} is the maximal reaction velocity, and K_{cat} is the catalytic constant that equals $V_{max}/[E]$.

In order to quantify the catalytic efficiency and understand the catalytic mechanism of the Pd−Ir cubes, we determined the apparent steady-state kinetic parameters for the reaction between TMB and H_2O_2 (see Methods for details). By plotting the initial reaction velocities against substrate concentrations, typical Michealis−Menten curves were observed for both TMB (Figure 3a) and H_2O_2 (Figure 3d). The curves were then fitted to the double-reciprocal or Lineweaver−Burk plots (Figure 3b,e),[22] from which the kinetic parameters shown in Table 1 were determined. For comparison, we also determined the kinetic parameters of 18 nm Pd cubic seeds (see Figure S5 for the kinetic assays) and listed those of HRP from literature[6] (Table 1). It can be seen that the K_{cat} value, which measures the efficiency of a catalyst, of the 19.2 nm Pd−Ir cubes is more than 20- and 400-fold higher than those of 18 nm Pd cubic seeds and HRP, respectively. To the best of our knowledge, the Pd−Ir cubes presented in this study show the highest catalytic efficiency in terms of K_{cat} compared to all the reported peroxidase mimics with comparable sizes. The K_m value of the Pd−Ir cubes was ~100-fold higher than that of HRP toward H_2O_2, suggesting that Pd−Ir cubes had a much lower affinity for H_2O_2 than HRP. Figure 3c and f show the double-reciprocal plots at different H_2O_2 and TMB concentrations, respectively. The lines in each plot are parallel, which is characteristic of a typical ping-pong mechanism as was observed for HRP.[23] This result indicated that, like HRP, the Pd−Ir cubes bind and react with one substrate (either TMB or H_2O_2) and then release a product before reacting with the other substrate.

Effect of Ir Content. Obviously, the enhanced activity of Pd−Ir cubes relative to the initial Pd seeds could be attributed to the coat of Ir shells. To better understand the role played by Ir shells in determining the catalytic efficiency, we prepared a set of Pd−Ir cubes with different molar ratios of Ir to Pd ($PdIr_x$) from the same batch of Pd seeds by adjusting the amount of Ir precursor introduced to the reaction solution (see Methods for details) and then evaluated their efficiencies. Figure 4 shows representative TEM images of these samples and compares their K_{cat} values. A thin Ir shell (with a darker contrast) over the Pd seed can be resolved from the TEM images, in which thickness gradually increases with Ir content. TEM images at a

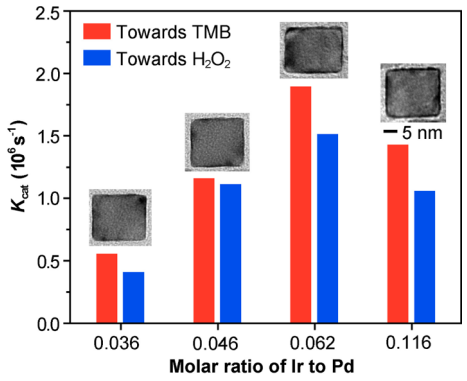

Figure 4. Effect of Ir content on the catalytic efficiency of Pd−Ir cubes prepared from 18 nm Pd cubic seeds. A histogram comparing the K_{cat} values of Pd−Ir cubes with different molar ratios of Ir to Pd. Height of each bar represents the average of three independent measurements. Insets are typical TEM images of the corresponding Pd−Ir cubes.

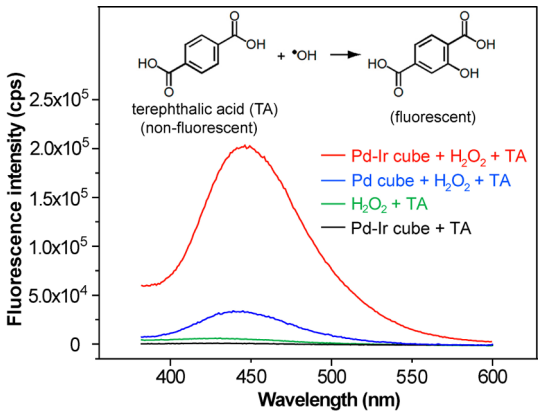

Figure 5. Detection of hydroxyl radical (·OH) generated from H_2O_2 using terephthalic acid (TA) as a probe. Fluorescence spectra taken from reaction solutions containing different reagents and catalysts as labeled on the spectra at reaction time t = 20 min. Concentrations: 0.5 mM TA, 0.2 M H_2O_2, and ~2 × 10^{10} particles/mL 19.2 nm Pd−Ir cubes (Figure 1) or 18 nm Pd cubes (Figure S1b) in 5 mL of 0.2 M NaOAc/HOAc buffer (pH 4.0, room temperature). Inset shows a scheme of the reaction between TA and ·OH.

lower magnification (Figure S6) suggest the good uniformities of all these samples. The K_{cat} values of the four different $PdIr_x$ samples (x = 0.036, 0.046, 0.062, and 0.116) toward both TMB and H_2O_2 showed a volcano-shaped dependence on the Ir contents, with maximum points corresponding to $PdIr_{0.062}$ (*i.e.*, the sample shown in Figure 1), which are around 4 times those of the $PdIr_{0.036}$. Deposition of more than 6.2% of Ir on the Pd seeds leads to a decrease in K_{cat} values.

Although the explicit mechanism of the peroxidase mimics-mediated catalytic reaction has yet to be revealed, generation of hydroxyl radicals (·OH) from H_2O_2 and the oxidation of TMB by ·OH to form the blue-colored complex (Figure 2b) were believed to be two key steps of this reaction according to previous studies.[7−15] To understand why the Ir-coated Pd cubes showed a better catalytic performance than the pristine Pd cubes, we compared their efficiencies in generating ·OH from H_2O_2 using terephthalic acid (TA) as a probe, which could easily react with ·OH to form a highly fluorescent 2-hydroxyterephthalic acid (inset of Figure 5).[24] In a typical procedure, 0.5 mM TA, 0.2 M H_2O_2, and ~2 × 10^{10} particles/mL 19.2 nm Pd−Ir cubes (sample shown in Figure 1) or 18 nm Pd cubes (sample shown in Figure S1b) were incubated in 5 mL of 0.2 M NaOAc/HOAc buffer (pH 4.0) for 20 min at room temperature, followed by fluorescence measurements using a spectrofluorometer. As shown in Figure 5, intense fluorescence was detected for solutions containing nanoparticles, H_2O_2, and TA, while very weak fluorescence signal was detected in the absence of either H_2O_2 or nanoparticles. This observation demonstrated that, for the present system, most of the ·OH species were generated from H_2O_2 in the presence of nanoparticles as catalysts. Significantly, the fluorescence intensity of the solution of Pd−Ir cubes, H_2O_2, and TA is much stronger than that of the solution of Pd cubes, H_2O_2, and TA. This result indicated that the Pd−Ir cubes were more efficient in generating ·OH from H_2O_2 than Pd cubes, which may be responsible for their superior catalytic performance toward the oxidation of TMB by H_2O_2 relative to Pd cubes.

TABLE 2. DFT-Calculated Adsorption Energies of Various Surface Species Likely Involved in the Oxidation of TMB by H_2O_2 on Different Model Surfaces[a]

	adsorption energies of surface species (eV)					
surface	H_2O_2	H_2O	·OH	·O	TMB	diimine
Pd(100)	−0.32	−0.26	−2.78	−4.31	−2.18	−2.80
Ir_{ML}/Pd(100)	−0.65	−0.40	−3.67	−5.50	−3.82	−4.88
Ir_{3ML}/Pd(100)	−0.56	−0.38	−3.32	−5.16	−2.84	−3.70
Ir(100)	−0.59	−0.41	−3.37	−5.16	−2.90	−3.76

[a] Diimine refers to the structure in the charge-transfer complex as shown in Figure 2b. Adsorption energies are calculated with respect to each adsorbate species in the gas phase.

To gain more insight into the enhanced catalytic activities of the Pd−Ir cubes, we also performed preliminary theoretical calculations (see Methods for details). Density functional theory (DFT)-based theoretical approaches have been shown to be powerful tools for generating mechanistic insights and thermodynamic and kinetic parameters that would otherwise be difficult to obtain.[25,26] It should be pointed out that, even though there are only two reactants (*i.e.*, H_2O_2 and TMB) in the reaction, a comprehensive analysis of the surface reaction mechanism and kinetics is well beyond the scope of the present work. Instead, we highlight the surface reactivities of different metallic surfaces to illustrate their intrinsic differences. Table 2 tabulates the adsorption energies of several key species in the reaction, including H_2O_2, H_2O, ·OH, TMB, and diimine on the four model surfaces: pure Pd(100) surface, single Ir overlayer on Pd(100) (designated Ir_{ML}/Pd(100)), three Ir

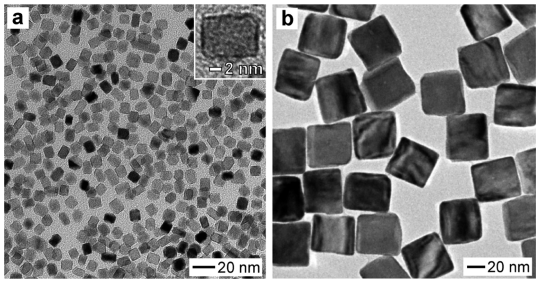

Figure 6. Size control of Pd−Ir cubes. TEM images of (a) 8.4 nm and (b) 52.2 nm Pd−Ir cubes that were grown from the 7.2 nm (Figure S1a) and 51 nm (Figure S1c) Pd cubic seeds, respectively. Inset in (a) shows a TEM image of an individual particle at a higher magnification.

overlayers on Pd(100) (Ir_{3ML}/Pd(100)), and pure Ir(100) surface. ·O is also included, as it may appear *via* ·OH disproportionation. The adsorption energies are consistently least exothermic on Pd(100) and most exothermic on Ir_{ML}/Pd(100), indicating that they are the least and most reactive of the four surfaces, respectively. Ir is known to be more reactive for adsorbing oxygen-containing species than Pd,[27] and expansive strain, as the Ir overlayers are held at the larger Pd lattice constant, tends to increase the surface reactivity of a transition metal.[28] Stronger adsorption of ·OH groups suggests that H_2O_2 dissociation into OH is likely more facile on the Ir shells than on Pd itself.[29] The fact that a single Ir overlayer on Pd(100) is more reactive than the thicker Ir overlayers indicates an additional ligand effect[30] stemming from the interaction of Ir monolayer with Pd substrate that enhances the reactivity of Ir_{ML}/Pd(100) but would be screened by thicker shells. Overall, these preliminary calculations are in good agreement with the experimental results shown in Figures 4 and 5 and Table 1. The Sabatier principle tells us that simply adsorbing molecules more strongly does not automatically make a surface more catalytically active. It may be anticipated that highly reactive surfaces, although they can dissociate H_2O_2 more easily,[27] could hamper the transfer of hydrogen from TMB to surface oxidant species and the desorption of the diimine product, and therefore reduce the overall activity. Evidently the Ir shells, at certain thicknesses, strike a much better balance between these two demands than pure Pd does. A numerical proof of this will be the subject of further research.

Size Control. It should be emphasized that the size of the Pd−Ir cubes could be readily controlled by coating Pd cubic seeds of different sizes with ~0.6 nm Ir shells. For instance, sub-10-nm Pd−Ir cubes with an average edge length of 8.4 nm (see Figure 6a) could be obtained by using Pd cubes of 7.2 nm in edge length as the seeds (Figure S1a). In addition, 52.2 nm Pd−Ir cubes (Figure 6b) could be prepared from Pd cubes of 51 nm in edge length as the seeds (Figure S1c). TEM images taken from these products indicate that the Pd−Ir cubes could be synthesized in high purity and good uniformity regardless of particle size. The steady-state kinetic assays of the 8.4 and 52.2 nm Pd−Ir cubes are shown in Figures S7 and S8, respectively, from which their kinetic parameters were determined. As compared in Table S2, the K_{cat} values of the 8.4, 19.2, and 52.2 nm Pd−Ir cubes were calculated to be roughly at levels of 10^5, 10^6, and 10^7 s^{-1}, respectively. This increase of K_{cat} with particle size may be ascribed to the fact that larger cubes have a greater surface area to interact with substrates. In this regard, it was not surprising that the three Pd−Ir cubes showed similar specific efficiencies (defined as the normalized K_{cat} to the surface area of an individual catalyst, K_{cat}/S) at a level of 10^2 s^{-1} nm^{-2} (Table S2).

It is worth noting that the molar ratios of Ir to Pd for the 8.4 and 52.2 nm Pd−Ir cubes shown in Figure 6 were determined to be 0.191 and 0.022, respectively, which correspond to approximate single Ir overlayers on both the 7.2 and 51 nm Pd cubic seeds. As shown in Figure S9a, deposition of less or more than 19.1% of Ir on the 7.2 nm Pd seeds led to a decrease in their catalytic activities. A similar trend was also observed for the 51 nm Pd seeds (Figure S9b).

Surface Modification. Taking advantage of the Ir-thiolate bonding,[31,32] we demonstrated that the surface of the Pd−Ir cubes could be easily modified with various functional groups such as −COOH and $-NH_2$ through the PEGylation of thiolated heterobifunctional polyethylene glycol (HS-PEG-R) chains (Figure 7; see Methods for experimental details). These functional groups on particle surfaces could serve as reactive sites to link various ligands such as peptides, nucleic acids, and antibodies (will discuss later). Importantly, the average number of PEG chains on each Pd−Ir cube could be conveniently quantified by subtracting the number of free PEG chains left in the supernatant (determined using the Ellman's test;[33] see Methods and Figure S10) from the total number of PEG chains added to the Pd−Ir cube suspension during PEGylation (Figure 7a; see Methods for details). Using Pd−Ir cube-S-PEG_{3400}-COOH and Pd−Ir cube-S-PEG_{3400}-NH_2 as model examples, we found that the catalytic activity of Pd−Ir cubes was well retained after they had been PEGylated with various numbers of PEG chains (Figure 7b). For instance, on average, the catalytic activity of a Pd−Ir cube decreased by only ~17% after it had been loaded with 200 -S-PEG_{3400}-NH_2 chains. It is worth noting that the maximum numbers of -S-PEG_{3400}-COOH and -S-PEG_{3400}-NH_2 chains loaded onto an individual Pd−Ir cube were determined to be ~3300 and ~4100, respectively. Therefore, the considerable retention of catalytic activities as shown in Figure 7b could be attributed to the relatively low loadings of PEG chains. These results indicate the simplicity and versatility of the Pd−Ir cubes in labeling ligands.

Application in Immunoassay. Finally, we applied the Pd−Ir cubes to the colorimetric enzyme-linked

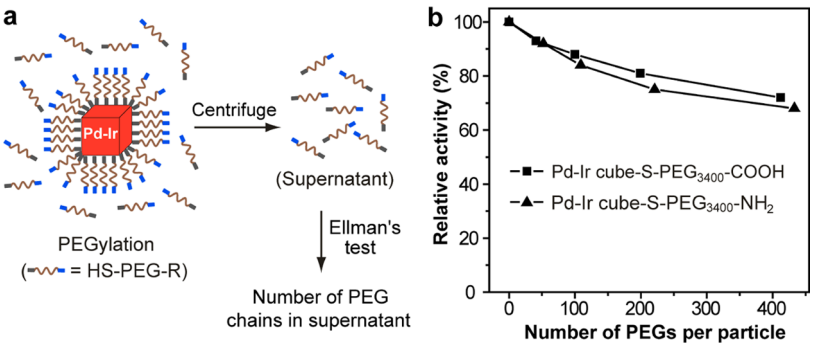

Figure 7. PEGylation of Pd−Ir cubes and the effect of PEG chain coverage on catalytic activity. (a) Schematics showing the PEGylation process and the method for quantifying PEG chains on the surface of Pd−Ir cubes. (b) Relative catalytic activities (*i.e.*, absorbance at 653 nm of reaction solutions at reaction time t = 5 min) of PEGylated 19.2 nm Pd−Ir cubes that were measured under standard conditions, in which the activity of pristine 19.2 nm Pd−Ir cubes was set as 100%. Datum at each point represents the average of three independent measurements.

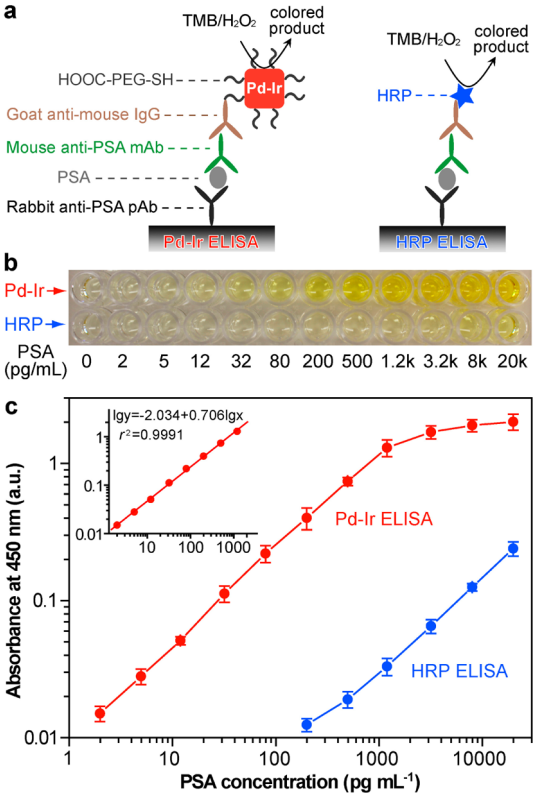

Figure 8. Detection of PSA with Pd−Ir cubes-based ELISA (Pd−Ir ELISA) and conventional HRP-based ELISA (HRP ELISA). (a) Schematics of the Pd−Ir and HRP ELISAs. (b) Representative photograph taken from the detection of PSA standards with Pd−Ir ELISA (top) and HRP ELISA (bottom);. (c) Corresponding calibration curves of the detection results shown in (b). Error bars indicate the standard deviations of six independent measurements. Inset shows the linear range region of the Pd−Ir ELISA.

immunosorbent assay (ELISA) of human PSA, a prostate cancer biomarker.[34,35] As shown in Figure 8a, the principle of the Pd−Ir ELISA is essentially the same as the conventional colorimetric HRP ELISA except for the substitution of HRP with Pd−Ir cubes. Here, the Pd−Ir cube−goat anti-mouse IgG conjugates were prepared from the 19.2 nm Pd−Ir cubes shown in Figure 1. In brief, the Pd−Ir cubes were first PEGylated with HS-PEG_{3400}-COOH. The resultant Pd−Ir cube-S-PEG_{3400}-COOH were then used to conjugate goat anti-mouse IgG through the EDC/NHS-mediated coupling reaction between the carboxyl groups on cubes and the primary amino groups on the antibodies[36] (see Figure S11 for methods and TEM images). For head-to-head comparison, we benchmarked the Pd−Ir ELISA against the conventional HRP ELISA by using the same set of antibodies and PSA standards. The procedures of both ELISAs were also kept the same (see Methods for details). PSA standards with various concentrations were monitored in a 96-well microtiter plate (Figure 8b) and subject to quantification using a plate reader, where the yellow-colored products (*i.e.*, diimine, $\lambda_{max} \approx 450$ nm) were generated by quenching the catalytic reaction using H_2SO_4.[23] A sigmoid curve regression between the logarithms of absorbance and PSA concentration was obtained for the Pd−Ir ELISA (red, Figure 8c). A quality linear relationship (r^2 = 0.9991) in the range 2−1200 pg/mL PSA was observed. The coefficient of variations across the entire concentration range was between 1.7% and 11.8% (n = 6), indicating a good reproducibility. The detection limit, defined as the concentration corresponding to a signal that is 3 times the standard deviation above the zero calibrator,[37] was calculated to be 0.67 pg/mL. In comparison, the detection limit of the HRP ELISA was determined to be 75 pg/mL based on its calibration curve (blue, Figure 8c), which is approximately 110-fold higher than that of Pd−Ir ELISA. This significant increase in detection sensitivity for the Pd−Ir ELISA could be mainly ascribed to the much higher catalytic efficiency of the Pd−Ir cubes relative to HRP because other conditions of both ELISAs were kept identical. The batch-to-batch reproducibility of the Pd−Ir ELISA was also evaluated by assaying a 50 pg/mL PSA standard using six different batches of Pd−Ir cubes (three duplicates for each batch; see Table S3), in which the coefficient of variation of the average absorbance at 450 nm was calculated to be 16.3%. These results suggest that the Pd−Ir ELISA is a

promising candidate for detection of disease biomarkers, which has a high sensitivity rivaling the limits of fluorescent and plasmonic methods[38−41] while retaining the simplicity and reliability of conventional colorimetric ELISA.

CONCLUSIONS

In summary, this work demonstrates a new type of peroxidase mimics that were prepared by coating Pd nanocubes with ultrathin Ir shells (a few atomic layers). Such peroxidase mimics feature high efficiency, good uniformity, controllable size, facile surface modification, and superior stability. Their potential application in disease diagnostics was demonstrated by the ultrasensitive colorimetric immunoassay of PSA. We believe the peroxidase mimic presented here may find widespread use in biomedicine and environmental protection in the near future.

METHODS

Chemicals and Materials. Sodium hexachloroiridate(III) hydrate ($Na_3IrCl_6 \cdot xH_2O$, MW = 473.9), sodium tetrachloropalladate(II) (Na_2PdCl_4, 98%), potassium bromide (KBr, ≥ 99%), L-ascorbic acid (AA, ≥ 99%), poly(vinylpyrrolidone) (PVP, MW ≈ 55 000), TMB, >99%, DAB, ≥99%, OPD, ≥98%, hydrogen peroxide solution (30 wt % in H_2O), acetic acid (HOAc, ≥99.7%), sodium acetate (NaOAc, ≥99%), PSA, ≥99%, Tween 20, bovine serum albumin (BSA, ≥98%), *N*-hydroxysulfosuccinimide sodium salt (NHS, ≥ 98%), terephthalic acid (TA, 98%), *N*-ethyl-*N*′-(3-(dimethylamino)propyl)carbodiimide hydrochloride (EDC, ≥99%), sodium chloride (NaCl, ≥99.5%), potassium chloride (KCl, ≥99%), sodium phosphate dibasic (Na_2HPO_4, ≥99%), potassium phosphate monobasic (KH_2PO_4, ≥99%), Tris base (≥99.9%), sodium azide (NaN_3, ≥99.5%), citric acid (99%), ethylenediaminetetraacetic acid (EDTA, ≥99%), 5,5′-dithiobis-(2-nitrobenzoic acid) (DTNB, ≥98%), and sulfuric acid (H_2SO_4, 95−98%) were all obtained from Sigma-Aldrich. Ethylene glycol (EG) was obtained from J. T. Baker, and HS-PEG_{3400}-COOH (MW ≈ 3400) and HS-PEG_{3400}-NH_2 (MW ≈ 3400) were obtained from Laysan Bio, Inc. Mouse anti-PSA monoclonal antibody (mouse anti-PSA mAb) and rabbit anti-PSA polyclonal antibody (rabbit anti-PSA pAb) were obtained from Abcam plc. Goat anti-mouse IgG and HRP-goat anti-mouse IgG conjugate were obtained from Thermo Fisher Scientific, Inc. Microtiter plates (96-well, polystryene, clear, flat botom) were obtained from Corning Inc. All aqueous solutions were prepared using deionized (DI) water with a resistivity of 18.0 MΩ·cm.

Preparation of Pd Nanocubes To Be Used as Seeds. *Pd Cubes of 7.2 and 18 nm.* Both Pd cubic seeds were synthesized using one-pot synthesis according to a previously reported procedure with minor modifications.[18] In brief, 8.0 mL of an aqueous solution containing 105 mg of PVP, 60 mg of AA, and different amounts of KBr and KCl (8 mg of KBr + 180 mg of KCl for 7.2 nm cubic seeds; 600 mg of KBr for 18 nm cubic seeds) was hosted in a vial and preheated at 80 °C in an oil bath under magnetic stirring for 10 min. Subsequently, 3.0 mL of a Na_2PdCl_4 aqueous solution (19 mg/mL) was added with a pipet. After the vial had been capped, the reaction was allowed to continue at 80 °C for 3 h. After being washed with DI water three times *via* centrifugation, the Pd cubic seeds were stored in 5 mL of EG for future use (~4 mg/mL in Pd element).

Pd Cubes of 51 nm. The 51 nm Pd cubes were synthesized using a seed-mediated growth, with the 18 nm Pd cubes above serving as seeds. Briefly, 12 mL of an aqueous solution containing 150 mg of PVP, 90 mg of AA, 450 mg of KBr, and 0.45 mL of the 18 nm Pd cubes was hosted in a 50 mL flask and preheated at 40 °C in an oil bath under magnetic stirring for 20 min. Then, 5 mL of Na_2PdCl_4 aqueous solution (19 mg/mL) was added with a pipet. After reacting for 24 h, the products were washed with DI water three times and redispersed in 2 mL of EG for future use (~18 mg/mL in Pd element).

Synthesis of Pd−Ir Cubes. *Pd−Ir cubes of 19.2 nm.* In a standard synthesis, 8 mL of an EG solution containing 100 mg of PVP and 50 mg of AA was hosted in a 25 mL three-neck flask and preheated to 200 °C in an oil bath under magnetic stirring for 10 min. Then, 1.0 mL of the 18 nm Pd cubic seeds was added to the flask using a pipet. After another 10 min, 4.0 mL of $Na_3IrCl_6 \cdot xH_2O$ solution (0.8 mg/mL, in EG) was injected to the flask at a rate of 1.0 mL/h using a syringe pump. The reaction was allowed to proceed for an additional 5 min after the complete injection of the $Na_3IrCl_6 \cdot xH_2O$ solution. The reaction was terminated by quickly placing the flask into an ice−water bath. The products were collected by centrifugation, washed once with acetone and twice with water, and finally redispersed in 1.0 mL of DI water for future use (~5.1×10^{13} particles/mL or ~8.5×10^{-8} M). The Pd−Ir cubes with different Ir contents (Figure 4) were obtained by taking a small amount (several drops) of the reaction solution with a glass pipet from a standard synthesis at different injection volumes of $Na_3IrCl_6 \cdot xH_2O$ solution.

Pd−Ir Cubes of 8.4 and 52.2 nm. The procedures for preparing the 8.4 and 52.2 nm Pd−Ir cubes were the same as the standard procedure for 19.2 nm Pd−Ir cubes except for the use of 0.4 mL of 7.2 nm Pd cubes and 0.6 mL of 51 nm Pd cubes as the seeds, respectively. The Pd−Ir cubes with different Ir contents (Figure S9) were obtained by taking a small amount of the reaction solution from the synthesis at different injection volumes of $Na_3IrCl_6 \cdot xH_2O$ solution.

Evaluation of the Peroxidase-like Activities of the 19.2 nm Pd−Ir Cubes. The experiments were conducted at room temperature in 1.5 mL tubes. For the oxidation of TMB by H_2O_2, the reactions were carried out in 1.0 mL of a 0.2 M NaOAc/HOAc buffer solution, pH 4.0, containing ~5×10^{-14} M Pd−Ir cubes as the catalysts and 2 M H_2O_2 and 0.8 mM TMB as the substrates. The reaction buffers for OPD and DAB were 0.2 M Na_2HPO_4 + 0.1 M citric acid and 0.1 M Tris-HCl + 0.15 M NaCl (pH 7.8), respectively. A photograph of the reaction solutions was taken at reaction time t = 5 min (see Figure 2).

For the measurements in Figure 2, the absorbance at 653 nm of the reaction solutions containing 3.4×10^{-14} M Pd−Ir cubes, TMB, and H_2O_2 in 0.2 M NaOAc/HOAc buffer at different conditions (pH, temperatures, TMB and H_2O_2 concentrations) was measured at t = 5 min (reaction time was recorded immediately after the mixture of Pd−Ir cubes and substrates). The catalytic activity of Pd−Ir cubes was characterized by the relative reactivity with the maximal absorbance being set as 100%.

Kinetic Assays. All steady-state kinetic assays were carried out at room temperature in 1.0 mL cuvettes with a path length (l) of 1.0 cm. Unless otherwise stated, a 0.2 M NaOAc/HOAc solution (pH 4.0) was used as the reaction buffer. Final concentrations of 1.4×10^{-12} M for the 18 nm Pd cubes, 2.2×10^{-13} M for the 8.4 nm Pd−Ir cubes, 3.4×10^{-14} M for the 19.2 nm Pd−Ir cubes, and 4.8×10^{-15} M for the 52.2 nm Pd−Ir cubes were used for their corresponding kinetic assay measurements. For the Pd−Ir cubes with different molar ratios of Ir to Pd (Figure 4), the final particle concentration was 3.4×10^{-14} M for their kinetic assay measurements. After addition of substrates (TMB and H_2O_2) in the buffer system containing cubes, the absorbance of the reaction solution at 653 nm of each sample was immediately measured as a function of time with intervals of 6 s using a spectrophotometer for 3 min. These "absorbance *vs* time" plots were then used to obtain the slope at the initial point ($Slope_{Initial}$) of each reaction by conducting the first derivation of each curve using OriginPro 9.0 software. The initial reaction velocity (v) was calculated by $Slope_{Initial}/(\varepsilon_{TMB\text{-}653\ nm} \times l)$, where $\varepsilon_{TMB\text{-}653\ nm}$ is the molar extinction coefficient of TMB

at 653 nm, which equals 3.9×10^4 $M^{-1} \cdot cm^{-1}$. The plots of v against substrate concentrations were fitted using nonlinear regression of the Michaelis–Menten equation. The apparent kinetic parameters were calculated based on the Michaelis–Menten equation $v = V_{max} \times [S]/(K_m + [S])$, where V_{max} represents the maximal reaction velocity, [*S*] is the concentration of substrate, and K_m is the Michaelis constant. Parameters K_m and V_{max} were obtained from the double reciprocal plot (or Lineweavere–Burk plot).[22]

PEGylation of 19.2 nm Pd–Ir Cubes and Quantification of PEG Chains on the Pd–Ir Cube. In a typical PEGylation process, 300 μL of an aqueous HS-PEG_{3400}-COOH or HS-PEG_{3400}-NH_2 solution at a specific concentration was added to 300 μL of an aqueous suspension of 19.2 nm Pd–Ir cubes (8.5×10^{-8} M). The mixture was incubated at room temperature with stirring for 3 h, followed by centrifuging at 14 000 rpm for 10 min. The supernatant was carefully collected and centrifuged two more times to remove the remaining Pd–Ir cubes. On the other hand, the precipitates (*i.e.*, Pd–Ir cube-S-PEG_{3400}-COOH or Pd–Ir cube-S-PEG_{3400}-NH_2) were washed three times with DI water and redispersed in 300 μL of DI water for future use.

The average number of PEG chains on each Pd–Ir cube was determined using the Ellman test (see Figure 7), in which thiol groups in PEG chains react with Ellman's reagent (*i.e.*, 5,5′-dithiobis(2-nitrobenzoic acid), DTNB) and generate yellow-colored products with maximum absorbance at 412 nm.[33] Prior to analysis, calibration curves (see Figure S10) were obtained from a series of HS-PEG_{3400}-COOH and HS-PEG_{3400}-NH_2 solutions with known concentrations (PEG standards). Briefly, 200 μL of PEG standards was mixed with 300 μL of phosphate buffer (0.3 M, pH 8.0, containing 1 mM EDTA) and 10 μL of Ellman's reagent (4 mg/mL, in 0.5 M phosphate buffer, pH 8.0, containing 1 mM EDTA). The mixture was allowed to react at room temperature for 15 min, and the absorbance at 412 nm was measured. Calibration curves were generated by plotting the absorbance at 412 nm against the PEG standard concentration. The concentration of free PEG chains in the supernatant of the PEGylation process was determined by comparing the absorbance intensity at 412 nm with the calibration curve and multiplying the dilution factors. The overall number of PEG chains on Pd–Ir cubes was obtained by subtracting the number of free PEG chains in the supernatant from the total PEG chains added to the PEGylation reaction solution. This number was then converted to the average number of PEG chains on each Pd–Ir cube by taking into account the total number of Pd–Ir cubes.[42]

Preparation of the Pd–Ir Cube–Goat Anti-Mouse IgG Conjugates. The Pd–Ir cube–goat anti-mouse IgG conjugates were prepared by labeling the Pd–Ir cube-S-PEG_{3400}-COOH (~200 -S-PEG_{3400}-COOH chains per cube) with anti-mouse IgG using EDC and NHS as coupling agents (see Figure S11a). In brief, 50 μL of Pd–Ir cube-S-PEG_{3400}-COOH (8.5×10^{-8} M, in DI water) was added to 450 μL of a 10 mM phosphate-buffered saline (PBS, pH 7.4) buffer at room temperature under stirring. Then, 5 μL of EDC (25 mM, in DI water) and 5 μL of NHS (50 mM, in DI water) were added. After 15 min, the particles were washed with DI water twice and redispersed in 50 μL of PBS. Subsequently, 50 μL of goat anti-mouse IgG (2 mg/mL, in PBS) was added to the particle suspension. After incubation at room temperature for 1 h, the reaction solution was put in a refrigerator overnight at 4 °C. Thereafter, 100 μL of blocking solution (5% BSA in PBS) was added to the reaction solution. After 2 h, the final products were collected by centrifugation, washed twice with PBS, and redispersed in 100 μL of PBS containing 1% BSA and 0.05% NaN_3 for future use.

Pd–Ir ELISA of PSA. The 96-well microtiter plates were coated with rabbit anti-PSA pAb (100 μL, 5 μg/mL in carbonate/bicarbonate buffer pH 9.6) at 4 °C overnight. After washing the plates three times with washing buffer (10 mM PBS pH 7.4 containing 0.5% Tween 20, PBST), the plates were blocked with 200 μL of blocking buffer (3% BSA in PBST) for 3 h at room temperature. The plates were then washed three times with washing buffer, followed by the addition of 100 μL of PSA standards in dilution buffer (1% BSA in PBST). After shaking at room temperature for 2 h, the plates were washed three times with washing buffer, and 100 μL of mouse anti-PSA mAb (2 μg/mL, in dilution buffer) was added. After 1 h shaking at room temperature, the plates were washed three times, and 100 μL of Pd–Ir cube–goat anti-mouse IgG conjugates (1:5000, in dilution buffer) was added, followed by 30 min shaking at room temperature. After washing four times, 100 μL of freshly prepared substrate solution (0.8 mM TMB and 2.0 M H_2O_2 in 0.2 M HOAc/NaOAc buffer, pH 4.0) was added. After 30 min incubation at room temperature, 50 μL of stop solution (2 M H_2SO_4) was added. The absorbance of each well at 450 nm was read using a microplate reader.

The procedure of HRP ELISA was the same as the Pd–Ir ELISA except for the substitutions of Pd–Ir cube–goat anti-mouse IgG conjugates with 100 μL of HRP-goat anti-mouse IgG conjugates (1 μg/mL, in dilution buffer) and the difference in the components of substrate solution (0.8 mM TMB and 5 mM H_2O_2 in citric acid/Na_2HPO_4 buffer, pH 5.0).

DFT Calculations. Spin-polarized periodic DFT calculations were performed in the generalized gradient approximation (GGA-PBE[43]) using the Vienna ab Initio Simulation Package.[44] The projector augmented wave (PAW) method was used to describe the core states,[45] and the Kohn–Sham valence states were expanded in a plane wave basis up to a kinetic energy of 400 eV. The equilibrium bulk lattice constants for Pd and Ir were calculated to be 3.95 and 3.88 Å, respectively, in good agreement with the experimental values (3.89 (Pd), 3.84 (Ir) Å).[46] Because the Pd cubes predominantly exhibited {100} facets, four *fcc*(100) surface models with different numbers of Ir overlayers were used. They included a pure Pd(100) surface, a single Ir overlayer on Pd(100) (designated Ir_{ML}/Pd(100)), three Ir overlayers on Pd(100) ($Ir_{3\ ML}$/Pd(100)), and a pure Ir(100) surface to represent even thicker Ir shells. As shown by the HAADF-STEM images in Figure 1c, the Ir shells were in nearly perfect registry with the Pd lattice, so all four surface models were based on the lattice constant of Pd. Thus, the Ir overlayers were laterally expanded by 1.8% compared to pure Ir. All four models consisted of four metal layers. The oxygen-containing species were modeled on a (2×2) surface unit cell, and the surface Brillouin zone was sampled with a $5 \times 5 \times 1$ Monkhorst–Pack *k*-point mesh. TMB and diimine were modeled on a (5×5) surface unit cell, and the surface Brillouin zone was sampled with a $3 \times 3 \times 1$ Monkhorst–Pack *k*-point mesh. The top two metal layers in the Pd(100) and Ir_{ML}/Pd(100) slabs and the top three metal layers (all Ir atoms) in the $Ir_{3\ ML}$/Pd(100) and Ir(100) slabs were fully relaxed. The remaining metal layer(s) was held fixed at bulk positions. Neighboring slabs in the *z* direction were separated by 9 metal layers equivalent of a vacuum. Adsorption was allowed on the relaxed side of each slab only, with dipole decoupling.[47] Adsorption energies were calculated as $\Delta E = E_{slab} + E_{mol} - E_{total}$, where E_{slab}, E_{mol}, and E_{total} are the energies of the clean surface without any adsorbate, the adsorbate molecule isolated in the gas phase in a neutral state (closed-shell or radical), and the surface with the adsorbate. The parameters including the cutoff energy, *k*-point density, and number of metal layers were chosen based on previous studies[48] to ensure convergence of the adsorption energies to 0.05 eV or less.

Characterizations. The UV–vis spectra were recorded using an Agilent Cary 60 UV–vis spectrophotometer. TEM images were taken using a JEOL JEM-2010 microscope operated at 200 kV. HAADF-STEM and EDX analyses were performed using a JEOL ARM200F with STEM Cs corrector operated at 200 kV. The concentrations of Pd and Ir ions were determined using ICP-AES (PerkinElmer Optima 7000DV), which could be converted to the particle concentration of Pd and Pd–Ir cubes once the particle size had been resolved by TEM imaging. The absorbance of samples in microtiter plates was read using a PerkinElmer Victor 3 1420 multilabel plate reader. Microtiter plates were shaken using a Corning LSE digital microplate shaker. pH values of buffer solutions were measured using an Oakton pH 700 benchtop meter. Photographs of samples in tubes and microplates were taken using a Canon EOS Rebel T5 digital camera. Fluorescence was measured using a Horiba Fluoromax-4 spectrofluorometer.

Conflict of Interest: The authors declare no competing financial interest.

Supporting Information Available: The Supporting Information is available free of charge on the ACS Publications website at DOI: 10.1021/acsnano.5b03525.

Electron microscopy images, plots, schematics, and tables (PDF)

Acknowledgment. This work was supported by the startup funds from Michigan Technological University (MTU). Theoretical work was performed at Louisiana State University (LSU) using high-performance computing resources provided by LSU and Oak Ridge National Laboratory and was in part supported by the Donors of the American Chemical Society Petroleum Research Fund and in part by the Center for Nanophase Materials Sciences, which is a DOE Office of Science User Facility. The authors are grateful to Ms. Jennifer Eikenberry of the School of Forest Resources and Environmental Science, MTU, for her assistance in ICP-AES analysis.

REFERENCES AND NOTES

1. Gaetani, G. F.; Galiano, S.; Canepa, L.; Ferraris, A. M.; Kirkman, H. N. Catalase and Glutathione Peroxidase Are Equally Active in Detoxification of Hydrogen Peroxide in Human Erythrocytes. *Blood* **1989**, *73*, 334–339.
2. Hiraga, S.; Sasaki, K.; Ito, H.; Ohashi, Y.; Matsui, H. A Large Family of Class III Plant Peroxidases. *Plant Cell Physiol.* **2001**, *42*, 462–468.
3. Price, C. P.; Newman, D. J., Eds. *Principles and Practice of Immunoassay*, 2nd ed.; Stockton: New York, 1997.
4. Klibanov, A. M.; Tu, T.; Scott, K. P. Peroxidase-Catalyzed Removal of Phenols from Coal-Conversion Waste Waters. *Science* **1983**, *221*, 259–261.
5. Wei, H.; Wang, E. Nanomaterials with Enzyme-Like Characteristics (Nanozymes): Next-Generation Artificial Enzymes. *Chem. Soc. Rev.* **2013**, *42*, 6060–6093.
6. Gao, L.; Zhuang, J.; Nie, L.; Zhang, J.; Zhang, Y.; Gu, N.; Wang, T.; Feng, J.; Yang, D.; Perrett, S.; et al. Intrinsic Peroxidase-Like Activity of Ferromagnetic Nanoparticles. *Nat. Nanotechnol.* **2007**, *2*, 577–583.
7. Song, Y.; Qu, K.; Zhao, C.; Ren, J.; Qu, X. Graphene Oxide: Intrinsic Peroxidase Catalytic Activity and Its Application to Glucose Detection. *Adv. Mater.* **2010**, *22*, 2206–2210.
8. He, W.; Wu, X.; Liu, J.; Hu, X.; Zhang, K.; Hou, S.; Zhou, W.; Xie, S. Design of AgM Bimetallic Alloy Nanostructures (M = Au, Pd, Pt) with Tunable Morphology and Peroxidase-Like Activity. *Chem. Mater.* **2010**, *22*, 2988–2944.
9. Jv, Y.; Li, B.; Cao, R. Positively-Charged Gold Nanoparticles as Peroxidiase Mimic and Their Application in Hydrogen Peroxide and Glucose Detection. *Chem. Commun.* **2010**, *46*, 8017–8019.
10. He, W.; Liu, Y.; Yuan, J.; Yin, J.; Wu, X.; Hu, X.; Zhang, K.; Liu, J.; Chen, C.; Ji, Y.; et al. Au@Pt Nanostructures as Oxidase and Peroxidase Mimetics for Use in Immunoassays. *Biomaterials* **2011**, *32*, 1139–1147.
11. André, R.; Natálio, F.; Humanes, M.; Leppin, J.; Heinze, K.; Wever, R.; Schröder, H.-C.; Müller, W.; Tremel, W. V_2O_5 Nanowires with an Intrinsic Peroxidase-Like Activity. *Adv. Funct. Mater.* **2011**, *21*, 501–509.
12. Sun, X.; Guo, S.; Chung, C.-S.; Zhu, W.; Sun, S. A Sensitive H_2O_2 Assay Based on Dumbbell-Like PtPd-Fe_3O_4 Nanoparticles. *Adv. Mater.* **2013**, *25*, 132–136.
13. Liu, M.; Zhao, H.; Chen, S.; Yu, H.; Quan, X. Interface Engineering Catalytic Graphene for Smart Colorimetric Biosensing. *ACS Nano* **2012**, *6*, 3142–3151.
14. Mu, J.; Wang, Y.; Zhao, M.; Zhang, L. Intrinsic Peroxidase-Like Activity and Catalase-Like Activity of Co_3O_4 Nanoparticles. *Chem. Commun.* **2012**, *48*, 2540–2542.
15. Gao, Z.; Hou, L.; Xu, M.; Tang, D. Enhanced Colorimetric Immunoassay Accompanying with Enzyme Cascade Amplification Strategy for Ultrasensitive Detection of Low-Abundance Protein. *Sci. Rep.* **2014**, *4*, 3966.
16. McKee, D. W. Catalytic Decomposition of Hydrogen Peroxide by Metals and Alloys of the Platinum Group. *J. Catal.* **1969**, *14*, 355–364.
17. Xia, X.; Figueroa-Cosme, L.; Tao, J.; Peng, H.-C.; Niu, G.; Zhu, Y.; Xia, Y. Facile Synthesis of Iridium Nanocrystals with Well-Controlled Facets Using Seed-Mediated Growth. *J. Am. Chem. Soc.* **2014**, *136*, 10878–10881.
18. Lim, B.; Jiang, M.; Tao, J.; Camargo, P. H. C.; Zhu, Y.; Xia, Y. Shape-Controlled Synthesis of Pd Nanocrystals in Aqueous Solutions. *Adv. Funct. Mater.* **2009**, *19*, 189–200.
19. Xia, X.; Xie, S.; Liu, M.; Peng, H.-C.; Lu, N.; Wang, J.; Kim, M. J.; Xia, Y. On the Role of Surface Diffusion in Determining the Shape or Morphology of Noble-Metal Nanocrystals. *Proc. Natl. Acad. Sci. U. S. A.* **2013**, *110*, 6669–6673.
20. Arblaster, J. W. Crystallographic Properties of Iridium. *Platinum Met. Rev.* **2010**, *54*, 93–102.
21. Josephy, P. D.; Eling, T. E.; Mason, R. P. The Horseradish Peroxidase-Catalyzed Oxidation of 3,5,3′,5′-Tetramethylbenzidine. Free Radical and Charge-Transfer Complex Intermediates. *J. Biol. Chem.* **1982**, *257*, 3669–3675.
22. Lineweaver, H.; Burk, D. The Determination of Enzyme Dissociation Constants. *J. Am. Chem. Soc.* **1934**, *56*, 658–666.
23. Porter, D. J. T.; Bright, J. H. The Horseradish Peroxidase-Catalyzed Oxidation of 3,5,3′,5′- Tetramethylbenzidine. *J. Biol. Chem.* **1982**, *258*, 9913–9924.
24. Ishibashi, K.; Fujishima, A.; Watanabe, T.; Hashimoto, K. Quantum Yields of Active Oxidative Species Formed on TiO_2 Photocatalyst. *J. Photochem. Photobiol., A* **2000**, *134*, 139–142.
25. Greeley, J.; Nørskov, J. K.; Mavrikakis, M. Electronic Structure and Catalysis on Metal Surfaces. *Annu. Rev. Phys. Chem.* **2002**, *53*, 319–348.
26. Hafner, J. Ab-Initio Simulations of Materials Using VASP: Density-Functional Theory and Beyond. *J. Comput. Chem.* **2008**, *29*, 2044–2078.
27. Ford, D. C.; Nilekar, A. U.; Xu, Y.; Mavrikakis, M. Partial and Complete Reduction of O_2 by Hydrogen on Transition Metal Surfaces. *Surf. Sci.* **2010**, *604*, 1565–1575.
28. Mavrikakis, M.; Hammer, B.; Nørskov, J. K. Effect of Strain on the Reactivity of Metal Surfaces. *Phys. Rev. Lett.* **1998**, *81*, 2819–2822.
29. Nørskov, J. K.; Bligaard, T.; Logadottir, A.; Bahn, S.; Hansen, L. B.; Bollinger, M.; Bengaard, H.; Hammer, B.; Sljivancanin, Z.; Mavrikakis, M.; et al. Universality in Heterogeneous Catalysis. 275−278. *J. Catal.* **2002**, *209*, 275–278.
30. Kitchin, J. R.; Nørskov, J. K.; Barteau, M. A.; Chen, J. G. Modification of the Surface Electronic and Chemical Properties of Pt(111) by Subsurface Transition Metals. *J. Chem. Phys.* **2004**, *120*, 10240–10246.
31. Yee, C. K.; Jordan, R.; Ulman, A.; White, H.; King, A.; Rafailovich, M.; Sokolov, J. Novel One-Phase Synthesis of Thiol-Functionalized Gold, Palladium, and Iridium Nanoparticles Using Superhydride. *Langmuir* **1999**, *15*, 3486–3491.
32. Love, J. C.; Estroff, L. A.; Kriebel, J. K.; Nuzzo, R. G.; Whitesides, G. M. Self-Assembled Monolayers of Thiolates on Metals as a Form of Nanotechnology. *Chem. Rev.* **2005**, *105*, 1103–1169.
33. Ellman, G. L. Tissue Sulfhydryl Groups. *Arch. Biochem. Biophys.* **1959**, *82*, 70–77.
34. Barry, M. J. Prostate-Specific-Antigen Testing for Early Diagnosis of Prostate Cancer. *N. Engl. J. Med.* **2001**, *344*, 1373–1377.
35. Lilja, H.; Ulmert, D.; Vickers, A. J. Prostate-Specific Antigen and Prostate Cancer: Prediction, Detection and Monitoring. *Nat. Rev. Cancer* **2008**, *8*, 268–278.
36. Qian, X.; Peng, X.-H.; Ansari, D. O.; Yin-Goen, Q.; Chen, G. Z.; Shin, D. M.; Yang, L.; Young, A. N.; Wang, M. D.; Nie, S. *In vivo* Tumor Targeting and Spectroscopic Detection with Surface-Enhanced Raman Nanoparticle Tags. *Nat. Biotechnol.* **2007**, *26*, 83–90.
37. Armbruster, D. A.; Tillman, M. D.; Hubbs, L. M. Limit of Detection (LQD)/Limit of Quantitation (LOQ): Comparison of the Empirical and the Statistical Methods Exemplified with GC-MS Assays of Abused Drugs. *Clin. Chem.* **1994**, *40*, 1233–1238.
38. Soukka, T.; Paukkunen, J.; Härmä, H.; Lönnberg, S.; Lindroos, H.; Lövgren, T. Supersensitive Time-Resolved Immunofluorometric Assay of Free Prostate-Specific Antigen with

Nanoparticle Label Technology. *Clin. Chem.* **2001**, *47*, 1269–1278.
39. Yu, F.; Persson, B.; Löfås, S.; Knoll, W. Surface Plasmon Fluorescence Immunoassay of Free Prostate-Specific Antigen in Human Plasma at the Femtomolar Level. *Anal. Chem.* **2004**, *76*, 6765–6770.
40. Su, L.-C.; Chen, R.-C.; Li, Y.-C.; Chang, Y.-F.; Lee, Y.-J.; Lee, C.-C.; Chou, C. Detection of Prostate-Specific Antigen with a Paired Surface Plasma Wave Biosensor. *Anal. Chem.* **2010**, *82*, 3714–3718.
41. Tabakman, S. M.; Lau, L.; Robinson, J. T.; Price, J.; Sherlock, S. P.; Wang, H.; Zhang, B.; Chen, Z.; Tangsombatvisit, S.; Jarrell, J. A.; et al. Plasmonic Substrates for Multiplexed Protein Microarrays with Femtomolar Sensitivity and Broad Dynamic Range. *Nat. Commun.* **2011**, *2*, 466.
42. Xia, X.; Yang, M.; Wang, Y.; Zheng, Y.; Li, Q.; Chen, J.; Xia, Y. Quantifying the Coverage Density of Poly(ethylene glycol) Chains on the Surface of Gold Nanostructures. *ACS Nano* **2012**, *6*, 512–522.
43. Perdew, J. P.; Burke, K.; Ernzerhof, M. Generalized Gradient Approximation Made Simple. *Phys. Rev. Lett.* **1996**, *77*, 3865–3868.
44. Kresse, G.; Furthmüller, J. Efficient Iterative Schemes for *ab initio* Total-Energy Calculations Using a Plane-Wave Basis Set. *Phys. Rev. B: Condens. Matter Mater. Phys.* **1996**, *54*, 11169–11186.
45. Kresse, G.; Joubert, D. From Ultrasoft Pseudopotentials to the Projector Augmented-Wave Method. *Phys. Rev. B: Condens. Matter Mater. Phys.* **1999**, *59*, 1758–1775.
46. Ashcroft, N. W.; Mermin, N. D. *Solid State Physics*; Saunders College: Orlando, FL, 1976.
47. Neugebauer, J.; Scheffler, M. Adsorbate-Substrate and Adsorbate-Adsorbate Interactions of Na and K Adlayers on Al(111). *Phys. Rev. B: Condens. Matter Mater. Phys.* **1992**, *46*, 16067–16080.
48. Silbaugh, T. L.; Giorgi, J. B.; Xu, Y.; Tillekaratne, A.; Zaera, F.; Campbell, C. T. Adsorption Energy of tert-Butyl on Pt(111) by Dissociation of tert-Butyl Iodide: Calorimetry and DFT. *J. Phys. Chem. C* **2014**, *118*, 427–438.

Note Added after ASAP Publication: This article published September 3, 2015 with an error in the first paragraph of the Kinetic Assays section. The corrected version published September 10, 2015.